Valley-dependent topological phase transition and quantum anomalous valley Hall effect in single-layer RuClBr

Hao Sun, Sheng-Shi Li, Wei-xiao Ji,* and Chang-Wen Zhang†
School of Physics and Technology, Institute of Spintronics, University of Jinan, Jinan, Shandong 250022, People's Republic of China

(Received 2 March 2022; revised 21 April 2022; accepted 26 April 2022; published 9 May 2022)

Quantum anomalous valley Hall effect (QAVHE), which combines both the features of QAHE and AVHE, is both fundamentally intriguing and practically appealing, but is experimentally challenging to realize in two-dimensional (2D) intrinsic magnetic materials to date. Here, based on first-principles calculations with the density functional theory $+U$ approach, we predicted the electronic correlation-driven valley-dependent quantum phase transition from ferrovalley (FV) to half-valley-semiconductor (HVS) to QAVHE to HVS to FV phase in single-layer RuClBr. Remarkably, the QAVHE phase with an integer Chern number ($C = 1$) and chiral spin-valley locking, which is induced by sign-reversible Berry curvature or band inversion between $d_{xy}/d_{x^2-y^2}$ and d_{z^2} orbitals, can achieve complete spin and valley polarizations for low-dissipation electronics devices. We also find that the electron valley polarization can be switched by reversing magnetization direction, providing a route of magnetic control of the valley degree of freedom. An effective $k \cdot p$ model is proposed to clarify valley-dependent quantum phenomena. Additionally, electronic correlation has an important effect on the variations of the Curie temperature of single-layer RuClBr. These findings shed light on the possible role of correlation effects on valley-dependent physics in 2D materials and open alternative perspectives for multifunctional spin-valley quantum devices in valleytronics.

DOI: 10.1103/PhysRevB.105.195112

I. INTRODUCTION

Recent advances in valleytronics are mainly related to the paradigm of the time-reversal symmetry ($\mathcal{T}$) connected valley, which generates novel valley-dependent transport phenomena and has attracted intensive attention [1,2]. To take advantage of the valley degree of freedom, valley polarization should be induced; several strategies have been proposed, such as optical pumping, magnetic field, magnetic proximity effects, and magnetic doping [3–12]. However, all these methods limit the valleytronics developments due to a very weak valley-polarization effect. In two-dimensional (2D) ferrovalley (FV) materials, such as 2H-VSe_2 [13], VSSe [14], GdI_2 [15], LaBrI [16], $GdCl_2$ [17], VClBr [18], Nb_3I_8 [19], $TiVI_6$ [20], NbX_2 (X = S, Se) [21], MXenes [22], and VSi_2N_4 [23], valley polarization occurs spontaneously because of the intrinsic $\mathcal{T}$ and spatial-inversion symmetry ($\mathcal{P}$) being broken together with spin-orbit coupling (SOC), which could facilitate the observation of the anomalous valley Hall effect (AVHE). Except for AVHE, the interplay between valley and band topology may enable the valley-polarized quantum anomalous Hall effect (VPQAHE) under zero magnetic field [24], which is highly promising for spintronic and quantum computational devices.

Compared with AVHE and QAHE, the combination of both of them, i.e., quantum anomalous valley Hall effect (QAVHE) [25–30], which has a nonzero Chern number ($C = 1$) and chiral spin-valley locking, is both fundamentally intriguing and practically appealing, due to its exotic valley-related physics and multifarious potential applications. Despite the progress made in AVHE and QAHE, the realization of QAVHE with high Curie temperature (T_C) in intrinsic ferromagnetic (FM) 2D materials is still rare. Therefore, it is still challenging and interesting to explore material candidates that can realize QAVHE with a high T_C for fixed system structures.

Here, based on first-principles calculations with the DFT $+U$ approach and the $k \cdot p$ model [25,30], the valley-dependent topological phase diagram has been predicted in single-layer (SL) magnetovalley (MV) coupled RuClBr. By manipulating MV coupling strength via the electron correlation effect (U), we found rich quantum states, covering the FV to half-valley-semimetal (HVS) to QAVHE to HVS to the FV phase. Remarkably, the QAVHE phase with $C = 1$ and chiral spin-valley locking, which is induced by sign-reversible Berry curvature or band inversion between $d_{xy}/d_{x^2-y^2}$ and d_{z^2} orbitals, can achieve complete spin-valley polarizations for low-dissipation electronics devices. We also find that the valley polarization can be switched by reversing magnetization, providing a route of magnetic control of the valley degree of freedom. Also, both the band gap and valley splitting of the MV phase in SL RuClBr are higher than the thermal energy of room temperature, which is key for device applications in valleytronics.

II. COMPUTATIONAL DETAILS

First-principles calculations have been performed using the Vienna *ab initio* simulation package (VASP), which is based on density-functional theory (DFT) [31–33].

*sps_jiwx@ujn.edu.cn
†ss_zhangchw@ujn.edu.cn

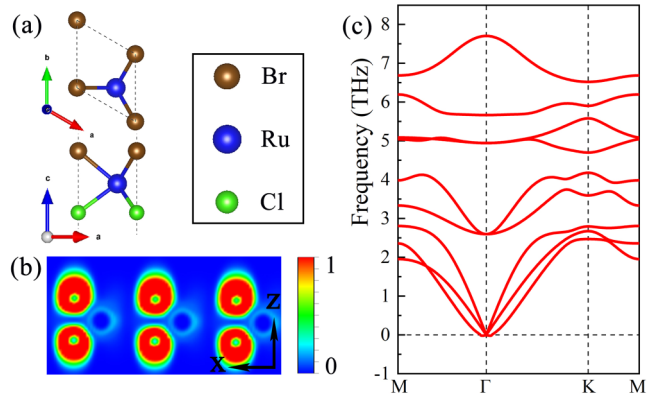

FIG. 1. (a) Top and side views of the crystal structure of SL RuClBr. (b) Electron localization function (ELF) along the x-z plane of SL RuClBr. (c) Phonon spectrum of SL RuClBr.

The Perdew-Burke-Ernzerhof (PBE) type generalized gradient approximation (GGA) is used to treat the exchange-correlation interaction between electrons [34]. The cutoff energy for the plane basis is 550 eV. The Brillouin zone is sampled with a Γ-center k mesh of size 17×17×1. All structures are fully optimized until the atomic force on each atom is less than 0.01 eV/ Å, and the energy convergence criteria are set to be 10^{-5} eV. A vacuum layer with a thickness of 20 Å is used to avoid interactions between periodically repeated layers. Phonon dispersion spectrum is calculated by using a 5×5×1 supercell and a 5×5×1 q grid based on the DFT perturbation theory to check the dynamical stability of SL RuClBr. The correlation effects for the Ru-4d electrons were treated by the DFT $+U$ method [35–37]. The Berry curvature is calculated by the maximally localized Wannier function method implemented in the WANNIER90 package [38,39]. The Chern numbers are calculated with the maximal localized Wannier function tight model by employing Cl p orbitals, Br p orbitals, and Ru d orbitals [40]. The edge states are studied by using the iterative Green's function method [41].

III. RESULTS AND DICUSSION

In analogy to the transition-metal dichalcogenides (TMDs), Janus SL RuClBr is composed of a Br-Ru-Cl sandwich layer, and each Ru atom has six nearest Cl and Br neighbors, as shown in Fig. 1(a). The optimized lattice constant of SL RuClBr is 3.56 Å, and the corresponding bond lengths of Ru-Cl and Ru-Br are 2.60 and 2.72 Å, respectively. In this case, the inequivalent bond lengths reduce the symmetry from D_{3h} to C_{3v} and break the mirror symmetry of SL RuClBr. To demonstrate the bonding character, we plot its electron localization function (ELF) in Fig. 1(b), in which the electrons are virtually localized over the Cl/Br and Ru atoms, indicating that SL RuClBr is a typical electride. Additionally, by calculating the phonon spectrum in Fig. 1(c), no imaginary frequency modes are observed, which demonstrates the SL RuClBr is dynamically stable.

To determine the magnetic ground state of SL RuClBr, we consider the energy differences of nonmagnetic (NM), FM, and antiferromagnetic (AFM) materials under different U. The corresponding magnetic configurations are shown in Fig. S1 of the Supplemental Material (SM) [42]. One can see that SL RuClBr always prefers the FM state with U ranging from 0 to 3 eV, with the magnetic moment on each Ru remaining 4.0 μ_B, due to the $\mathcal{T}$ being broken. According to the Mermin-Wagner theorem [43], stable FM coupling is forbidden in the 2D isotropic Heisenberg model. However, finite magnetic anisotropy can protect long-range FM order, so the stability of FM order in SL RuClBr strongly correlates with its magnetic anisotropy energy (MAE); MAE $= E_{x/y} - E_z$, which is defined as the energy difference between in-plane (IP) and out of plane (OP) magnetization. If the MAE is positive, it means that the energy along the OP direction is lower than the energy along the IP direction; thus the MAE is along the OP direction. We plot the energy difference MAE with U as the horizontal axis (Fig. S2 in the SM [42]). When $U < 2.23$ eV, SL RuClBr prefers an OPFM state; when $U > 2.23$ eV, it is in the IPFM state. The T_C can be estimated by employing Monte Carlo (MC) simulations based on the effective classical spin model expressed as

$$H = -\sum_{i,j} J_{ij} S_i \left[S_j - K \sum_i \left(S_i^z\right)^2 \right], \tag{1}$$

where S_i is the spin vector on the Ru site i, J_{ij} is the exchange coupling constant between sites i and j, and K is the on-site magnetic anisotropy. For rough estimation, we include only the nearest-neighbor (NN) coupling J in the model, where positive (negative) K corresponds to OP (IP) anisotropy. In order to extract the exchange coupling parameter J in the MC model, we compare the energies of FM and AFM configuration (Figs. S1(b) and S1(c) [42]). The corresponding energies in the spin model are given by

$$E_{\mathrm{FM}} = E_0 - 6J|S|^2 - K|S^z|^2, \tag{2}$$

$$E_{\mathrm{AFM}} = E_0 + 2J|S|^2 - K|S^z|^2. \tag{3}$$

Thus,

$$J = \frac{E_{\mathrm{AFM}} - E_{\mathrm{FM}}}{8|S|^2}, \quad K = \frac{E(100) - E(001)}{|S|^2}, \tag{4}$$

in which E_0 is the energy without magnetic coupling. From Eq. (4), we can obtain that $J = 5.8$ meV and $K = 104.8$ μeV for $U = 1.5$ eV; $J = 3.3$ meV and $K = 112.2$ μeV for $U = 2.05$ eV; $J = 2.7$ meV and $K = 13.4$ μeV for $U = 2.2$ eV. Figure 2 presents the diagram of simulated magnetization via temperature. We find that $T_C = 848$ K for $U = 1.5$ eV; $T_C = 484$ K for $U = 2.05$ eV; and $T_C = 394$ K for $U = 2.20$ eV, which is favorable to practical application in valleytronics.

Electronic correlation has a significant impact on the magnetic, topological, and valley features in 2D FM materials [27]. To show the valley dependence of topological phase (TP) transitions on electronic properties, we present the evolution of electronic band structures driven by electronic correlation (U) in SL RuClBr, and the obtained phase diagram is illustrated in Fig. 3. The representative electronic band structures without and with SOC, and the evolution mechanism of the energy band gap induced by different U are plotted in Figs. S3–S5 [42], respectively.

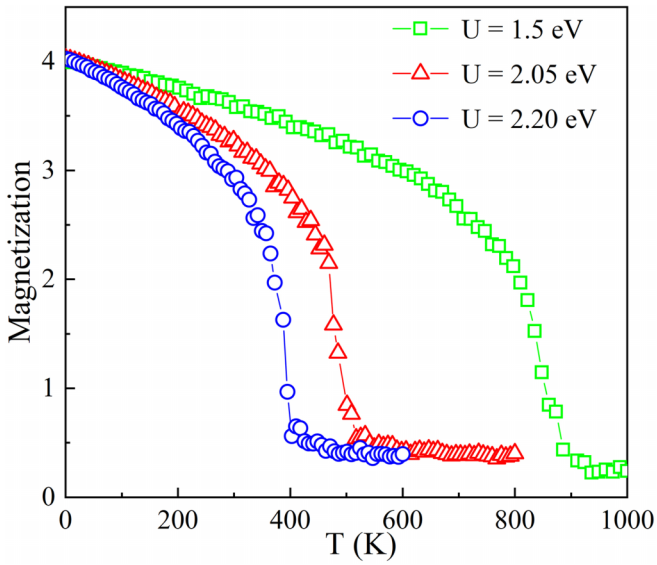

FIG. 2. Normalized magnetic moment as a function of temperature by MC simulations with different U.

Regarding a small U ($U = 0$eV), SL RuClBr is a fully spin-polarized semiconductor with a small indirect band gap. The edge of the conduction band (CB) with d_{z^2} orbital at the K/K' valleys is mainly composed of the spin-down channel, whereas the edge of the valence band (VB) is from spin-up d_{xz}/d_{yz} orbitals (Fig. 4(a) and Fig. S3(a) in the SM [42]), which indicates a bipolar magnetic semiconductor (BMS) character. With increasing U, the edge of the VB with Ru $d_{xy}/d_{x^2-y^2}$ moves up relative to the original Ru d_{xz} and Ru d_{yz} bands; when U ranges from 1 to 1.93 eV, the global band gap starts to decrease [Fig. 5(a)], forming a pair of Dirac-type valleys at the edge of the VB [Fig. 6(a)], where Dirac-type valleys mean that two valleys at the K and K' points form a pair of valleys shaped like Dirac cones, similar to that of SL MoS_2 [44–46]. On account of $\mathcal{T}$ and $\mathcal{P}$ being broken, both the edges of the CB and VB here belong to the same (i.e., spin-down) channel, forming a FV state with a giant valley splitting of 225.1 (18.6) meV at the VB (CB) edge [Fig. 6(b)]. When considering SOC, the electron wave function is a spinor with an upper spin component and a lower spin component, so we can project the wave function onto both components.

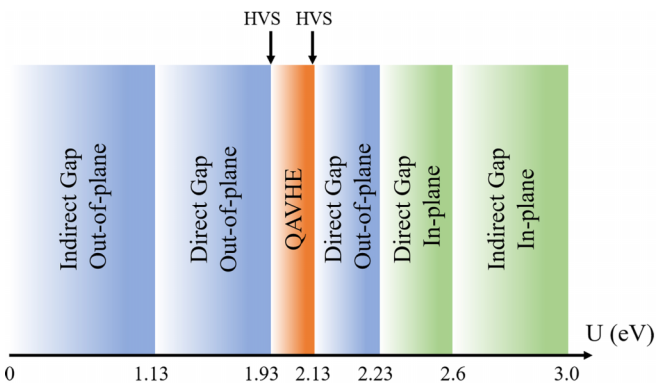

FIG. 3. Phase diagram for SL RuClBr with different U values.

Therefore, AVHE with an anomalous velocity $v_a \sim -\frac{e}{\hbar}E \times \Omega$ can be clearly observed [Figs. 6(e) and (6f)] [47].

To clarify MV coupling physics in SL RuClBr, we introduce a TB model to explain the valley-dependent quantum state. Take $U = 1.5$ eV as an example; the edge of the VB and CB are determined by different orbital components. The edge of the CB is composed of a Ru d_{z^2} orbital, where the edge of the VB is mainly by the Ru $d_{xy}/d_{x^2-y^2}$ orbitals. Since the wave-vector symmetry is C_{3v} at the K/K' valleys, the basis function could be expressed as $|\varphi_c^\tau\rangle = |d_{z^2}\rangle$ and $|\varphi_v^\tau\rangle = \sqrt{\frac{1}{2}}(|d_{x^2-y^2}\rangle + i\tau|d_{xy}\rangle)$, where $\tau = \pm 1$ donated the valley Index. The subscripts v and c represent the valley state at the edges of the VB and CB, respectively. The effect of SOC on the edges of the VB and CB state may be approximated as $\hat{H}_{\rm SOC} = \hat{H}^0_{\rm SOC} + \hat{H}^1_{\rm SOC}$ [19,48,49], where $\hat{H}^0_{\rm SOC}$ represents the interactions between the same spin channel, and $\hat{H}^1_{\rm SOC}$ corresponds to the opposite spin state. Considering strong magnetic exchange interaction, the opposite spin states are separated effectively, so $\hat{H}^1_{\rm SOC}$ could be ignored in this work. Hence, $\hat{H}_{\rm SOC}$ takes the form

$$\begin{aligned}\hat{H}_{\rm SOC} &\approx \hat{H}^0_{\rm SOC} \\ &= \lambda\hat{S}_z\big(\hat{L}_z\cos\theta + \tfrac{1}{2}\hat{L}_+e^{-i\phi}\sin\theta + \tfrac{1}{2}\hat{L}_-e^{+i\phi}\sin\theta\big), \quad (5)\end{aligned}$$

where $\hat{S}$ and $\hat{L}$ represent the spin and orbital angular momentums, respectively. θ and ϕ are the polar angles of spin orientation. As MAE is in the OP, Eq. (5) can be simplified as $\hat{H}_{\rm SOC} = \lambda\hat{S}_z\hat{L}_z = \alpha\hat{L}_z$, where $\alpha = \pm\frac{1}{2}\lambda$, suggesting that the Hamiltonian $\hat{H}_{\rm SOC}$ relies on the orbital angular momentum $\hat{L}_z$. The resulting energy shifts for the valence band maximum (VBM) and conduction band minimum (CBM) at the two valleys are given by $E_v^\tau = \langle\varphi_v^\tau|\hat{H}_{\rm SOC}|\varphi_v^\tau\rangle$ and $E_c^\tau = \langle\varphi_c^\tau|\hat{H}_{\rm SOC}|\varphi_c^\tau\rangle$, respectively. Hence, the valence (conduction) energy difference ΔE_v (ΔE_c) at the K/K' valleys can be expressed as

$$\begin{aligned}\Delta E_v &= E_v^- - E_v^+ \\ &= i\langle d_{xy}|\hat{H}_{\rm SOC}|d_{x^2-y^2}\rangle - i\langle d_{x^2-y^2}||\hat{H}_{\rm SOC}|d_{xy}\rangle, \quad (6)\end{aligned}$$

$$\Delta E_c = E_c^- - E_c^+ = 0. \quad (7)$$

From Eq. (6), we can obtain $\Delta E_v = -4\alpha$. This indicates that valley polarization significantly occurs at the edge of the VB but not the CB, which is line with our DFT calculations [Fig. 6(c)). Furthermore, valley polarization for electrons can be switched by reversing magnetization orientation, which is confirmed by DFT results in Fig. 6(d). Since the low-energy bands at the K/K' valleys belong to the spin-down channel, the spin polarization of carriers is simultaneously switched. From practice, using the intrinsic magnetism rather than the applied magnetic field allows a nonvolatile scheme for generating valley polarization. Also, magnetism can be controlled in a fully electric manner, e.g., by using current pulses through spin torques [50], which is desired for device applications. Thus, the intrinsic FV physics discussed here offers a route for controlling the valley and spin degrees of freedom.

Our most prominent finding is that SL RuClBr is a promising MV-coupled material, which can host various correlation-driven TP diagrams starting from the FV phase

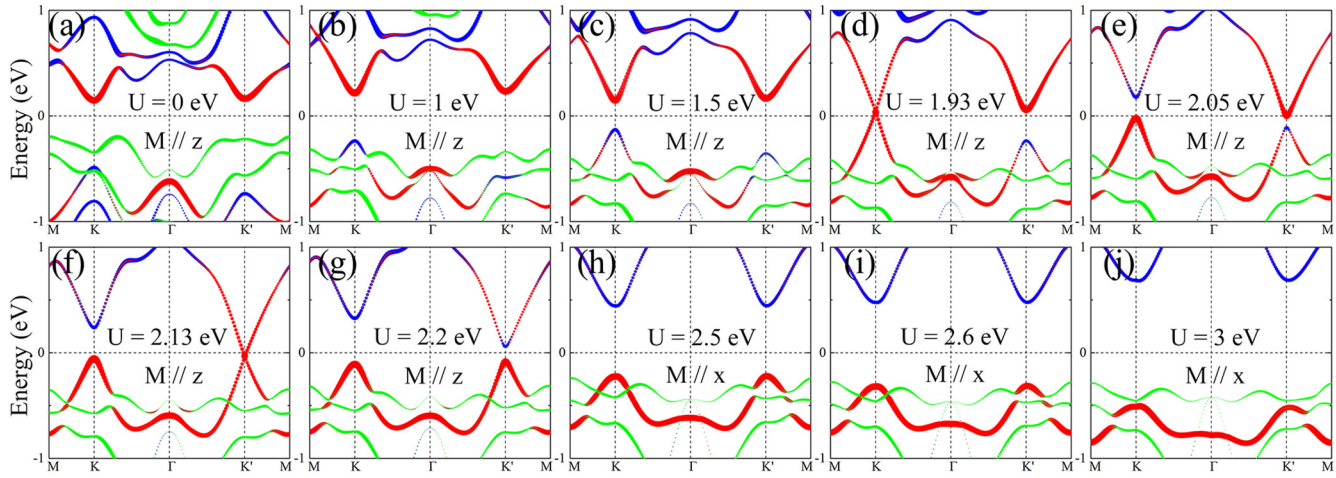

FIG. 4. Orbital-projected band structures of SL RuClBr obtained from GGA+SOC $+U$ (U varies from 0 to 3 eV). The blue circle represents components of Ru d_{xy} and Ru $d_{x^2-y^2}$ orbitals, the red one is for the component of the Ru d_{z^2} orbital, and the green one represents Ru d_{xz} and Ru d_{yz}, respectively.

(Fig. 3). Such a FV state is highly favorable to generating, transporting, and manipulating spin currents in spin-valley spintronics. By further increasing electronic correlation U, the band gap at the K valley decreases, while the other one at the K' valley is reduced as well, as is shown in Fig. 5(c). During the transition, a critical state, namely, the HVS state, appears at $U = 1.93$ eV, where the band gap closes at the K valley and the other K' valley is still in semiconductor status. The gapless crossing point is twofold degenerate with linear dispersion, similar to that of Weyl semimetals [51]. Here, since the SOC effect is already considered, the HVS is a true Dirac half-metal with 100% spin polarization [52], which provides mass-free electron mobility, in favor of charge and spin transport. After the critical state we further increase U ($U > 1.93$ eV), and the Ru $d_{xy}/d_{x^2-y^2}$ bands continue to move up, while bands of the Ru d_{z^2} component go down at both of the two valleys. In this way, the edges of the CB and VB are in the process of getting closed at the K' valley, but at the K valley, the CB and VB are apart from each other and, hence, orbitals of $d_{xy}/d_{x^2-y^2}$ from the VB interchange to CB at the K valley. This gap close-reopen scenario and interchanging of orbital composition indicates a transition from trivial to nontrivial TP. Interestingly, when $U = 2.13$ eV, another HVS state is inevitably encountered, with the band gap closing and reopening again at the K' valley, but is gapped at the K valley [Figs. 4(f) and 5(c)]. While for $U > 2.13$ eV, a new FV state appears, and the Ru d_{z^2} of the edge of the CB has been swapped with Ru $d_{xy}/d_{x^2-y^2}$ orbitals of the edge of the VB at the K' valley. In this case, there is a new FV state with a giant valley splitting of 267.3 (23.8) meV at the edge of the CB (VB) (Fig. S4 in the SM [42]).

Remarkably, the sign-reversible valley-dependent Berry phase effect occurs in regions when U variates. To demonstrate this phenomenon, we evaluate the intrinsic anomalous Hall conductivity σ_{xy}^{i} [53,54]:

$$\sigma_{xy}^{i} = -\frac{e^2}{h}\frac{1}{2\pi}\int_{\mathrm{BZ}} d^2k\Omega_z(k). \tag{8}$$

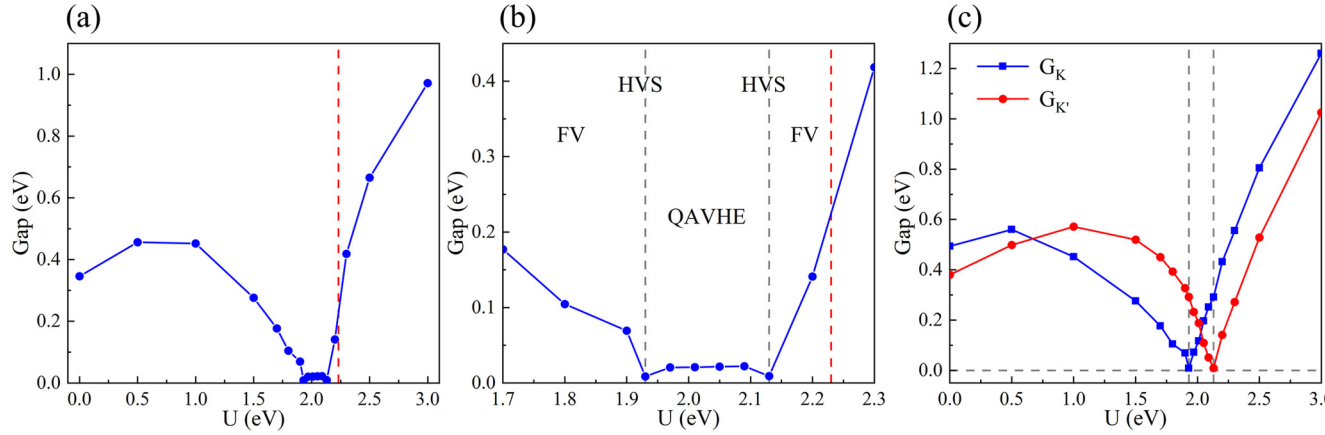

FIG. 5. (a) Global band gaps as a function of U (0–3 eV). (b) Enlarged view of the left plane between $U = 1.7$ and 2.3 eV, with a phase diagram shown with different U. (c) Band gaps for K/K' valleys when the magnetization is along the z direction. The vertical red dotted line represents MAE changes from OP to IP.

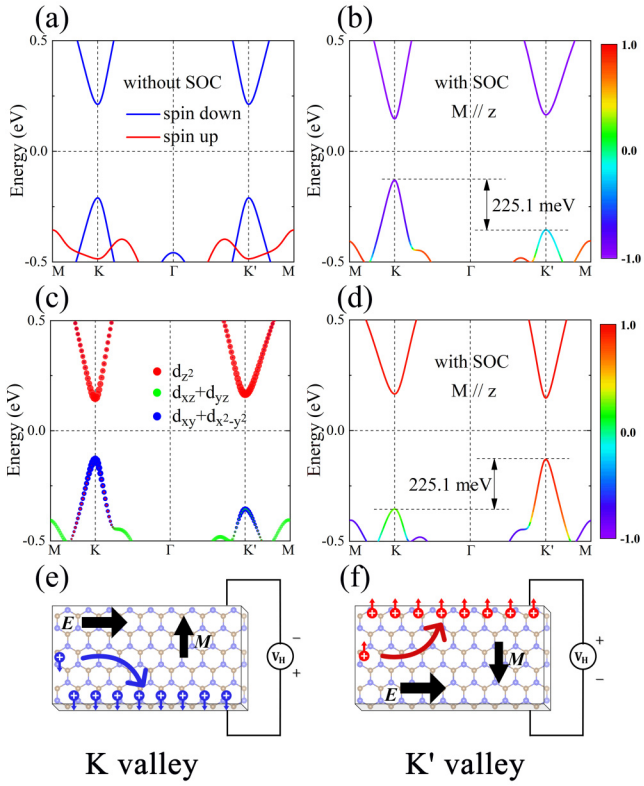

FIG. 6. Band structure of SL RuClBr with $U = 1.50$ eV: (a) DFT $+U$ and (b) DFT $+U+$ SOC. Here, the magnetization is along the $+z$ direction. (c) Orbital-projected band structure for the case in (b). (d) Band structure of SL RuClBr when the magnetization is switched to the $-z$ direction. The red and blue colors in (a)–(d) indicate the spin-up and spin-down bands, respectively. (e) Schematic diagram of AVHE for the hole-doped case. The magnetic moment is along the $+z$ direction. Panel (f) is the same as (e) but with opposite magnetization. The red and blue spheres in (e), (f) denote the spin-up and spin-down components, respectively.

The Berry curvature $\Omega_z(k)$ of the 2D system can be expressed by

$$\Omega_z(k) = -2\mathrm{Im}\sum_{n'\neq n} f_{nk}\frac{\langle nk|v_x|n'k\rangle\langle n'k|v_y|nk\rangle}{(\omega_{n'}-\omega_n)^2}, \qquad (9)$$

where the summation is over both band indices n and n' with n restricted to all occupied bands, $\varepsilon_n = \hbar\omega_n$ is the energy, and v_x and v_y are velocity operators in the x and y directions, respectively. f_{nk} is the Fermi distribution function. Figure 7 shows the Berry curvatures with $U = 1.5$ eV (a), 2.05 eV (b), and 2.2 eV (c), respectively.

The TP diagram is closely related to the sign-reversible valley-dependent Berry phase effect. Regarding the FV state ($U = 1.50$ eV), for which the k-resolved Berry curvature $\Omega_z(k)$ is shown in Fig. 7(a), a nonzero Berry curvature occurs around K/K' valleys with opposite signs and different magnitudes at K/K' valleys. When $U = 1.93$ eV, the FV state experiences a TP transition into the QAHVE state, bridged by a HVS state. Within $U = 2.05$ eV, the sign of $\Omega_z(k)$ at the K valley flips [Fig. 7(b)]. Further increasing $U = 2.13$ eV, the K' valley also experiences a TP transition, akin to the case of the

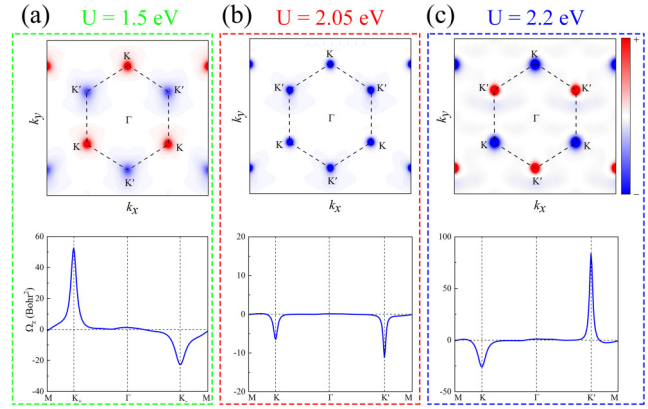

FIG. 7. Berry curvature of SL RuClBr with $U = 1.50$ eV (a), 2.05 eV (b), and 2.2 eV (c). The top planes are a contour map of Berry curvature in the whole 2D BZ; the bottom planes are Berry curvature along the high-symmetry points.

K valley, resulting in the sign change of $\Omega_z(k)$ at the K' valley. With the increase of U, it transforms from HVS to another FV state. By comparing these two FV states, the sign of Berry curvature at the K and K' valleys are quite opposite [Figs. 7(a) and 7(c)]. Such dynamics of Berry curvature $\Omega_z(k)$ is bound to influence valley-related anomalous transport phenomena such as AHVE, valley Nernst effect, valley magneto-optical Kerr effect, and valley magneto-optical Faraday effect [30].

It is remarkable that there is a change of sign for the Berry curvature at the K and K' valleys, which contribute opposite and half quantized Hall conductivity, $e^2/2h$ and $-e^2/2h$, respectively. The topological phase transition of K and K' happens at two different critical on-site Coulomb interactions: When $U < 1.93$ eV, $C = 1/2 - 1/2 = 0$; when $U > 2.13$ eV, $C = -1/2 + 1/2 = 0$, while in the case of 1.93 eV $< U <$ 2.13 eV, Berry curvature at one of the two valleys changes its sign and leads to a total Chern number C as $1/2 + 1/2 = 1$. The U of the QAHVE phase is mainly distributed from 1.93 to 2.13 eV, which can be illustrated by the calculated Berry curvatures in BZ space [Fig. 7(b)]. Specially, we find that the Berry phase takes the same signs but not identical absolute values at the K and K' valleys. By integrating Berry curvature $\Omega_z(k)$ in the whole region, we obtain a quantized AHC e^2/h [Fig. 8(c)], indicating the nontrivial topology with $C = 1$. Also, the edge spectrum calculated with the WANNIER90 package [38,39] in Fig. 8(d) shows a single gapless chiral state connecting the conduction and valence bands, which is consistent with quantized AHC e^2/h. This unique quantum state can be detected by using the noncontact magneto-optical technique [55], and thus is of key importance for most practical applications in valleytronics.

Finally, we must emphasize that the exotic QAVHE phase observed here coexists with a valley index and QAHE, but is different from the separated AVHE and QAHE phases. This leads to several interesting features. First, the gapless chiral edge band of emphasis QAVHE phase acquires a valley character. As shown in Fig. 8(d), the edge states belong to the K/K' valley, which is promising for valleytronics devices. Second, the boundaries of the QAVHE phase at $U = 1.93$ and 2.13 eV are critical points of TP transitions, which belong

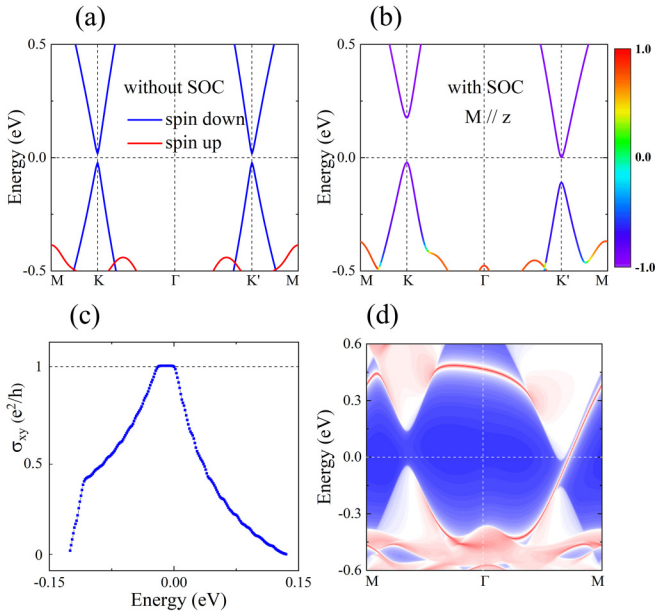

FIG. 8. Band structure of SL RuClBr with $U = 2.05$ eV (a) without SOC and (b) with SOC. (c) Anomalous Hall conductivity versus chemical potential for the case in (b). (d) The corresponding edge spectrum for the QAVHE state with $U = 2.05$ eV.

to the HVS state. As mentioned above, the common characteristic of the HVS phase has the band gap closed only at one of the two K/K' valleys. In this respect, the transport in the bulk would also be fully valley polarized. Additionally, the QAVHE is different from conventional VPQAHE [24]. First, the QAVHE is caused by unbalanced Berry curvature at the K and K' valleys, and combines both the valley index and QAHE. It is characterized by an integer Chern number $C(= C_K + C_{K'})$, but has a noninteger valley Chern number $C_v(= C_K – C_{K'})$. As for VPQAHE, both the Chern number C and valley Chern number C_v are integer, where the K and K' are the two valleys of the honeycomb lattice. Second, from the edge state point of view, the edge states of QAVHE are linked by different valleys, while the edge states of VPQAHE are linked by the same valley, i.e., the C originates from only one valley. Third, except for SL RuClBr, these valley-dependent TP diagrams can also be observed in SL $FeBr_2$, FeClBr, FeI_2, FeClI, FeBrI, and $RuCl_2$ (Figs. S5–S11 in the SM [42]), which greatly expands this family of FV materials with QAHE.

IV. CONCLUSIONS

To summarize, based on first-principles calculations with the DFT $+U$ approach, we found electronic correlation-driven valley-controlled TP transition from FV to HVS to QAVHE to HVS to FV phase in SL RuClBr. Remarkably, QAVHE with $C = 1$ and chiral spin-valley locking, which is induced by sign-reversible Berry curvature or band inversion between $d_{xy}/d_{x^2-y^2}$ and d_{z^2} orbitals, can achieve complete spin and valley polarizations for low-dissipation electronics devices. We also find that this electron valley polarization can be switched by reversing the magnetization direction, providing a route of magnetic control of the valley degree of freedom. A $k \cdot p$ model is further constructed to make out the FV feature. At present, the control of on-site Coulomb interactions is challenging in experiments, nut for 2D materials, we can indirectly change the strain to achieve the same effect as changing U, and thus achieve the purpose of tuning U. We believe that with further study, there will be a deeper understanding of the regulation of U. For now, it is valuable and worthwhile to find exotic topological phase transitions driven by the electronic correlation effect based on regulation of U, and our work emphasizes the importance of electronic correlation, and enriches the research on QAVHE. Recent experiments have proposed that the magnetism of the 2D ferromagnets can be controlled by strain, gating, and external magnetic fields, which can further stimulate the study of tunable topological valley polarization and valley-dependent QAHVE. Therefore, our work provides a desirable platform utilizing electronic correlation to control topological spin-valley devices for spintronic and valleytronic applications in the future.

ACKNOWLEDGMENTS

This work was supported by the Taishan Scholar Program of Shandong Province (Grant No. ts20190939), Independent Cultivation Program of Innovation Team of Jinan City (Grant No. 2021GXRC043), National Natural Science Foundation of China (Grant No. 12004137) and National Natural Science Foundation of China (Grant No. 52173283).

[1] J. R. Schaibley, H. Y. Yu, G. Clark, P. Rivera, J. S. Ross, K. L. Seyler, W. Yao, and X. D. Xu, Nat. Rev. Mater. **1**, 16055 (2016).
[2] A. Rycerz, J. Tworzydło, and C. W. J. Beenakker, Nat. Phys. **3**, 172 (2007).
[3] H. Zeng, J. Dai, W. Yao, D. Xiao, and X. Cui, Nat. Nanotechnol. **7**, 490 (2012).
[4] K. F. Mak, K. He, J. Shan, and T. F. Heinz, Nat. Nanotechnol. **7**, 494 (2012).
[5] Z. L. Ye, D. Z. Sun, and T. F. Heinz, Nat. Phys. **13**, 26 (2017).
[6] T. Cai, S. A. Yang, X. Li, F. Zhang, J. Shi, W. Yao, and Q. Niu, Phys. Rev. B **88**, 115140 (2013).
[7] L. Xu, M. Yang, L. Shen, J. Zhou, T. Zhu, and Y. P. Feng, Phys. Rev. B **97**, 041405(R) (2018).
[8] K. L. Seyler, D. Zhong, B. Huang, X. Linpeng, N. P. Wilson, T. Taniguchi, K. Watanabe, W. Yao, D. Xiao, M. A. McGuire, K. C. Fu, and X. Xu, Nano Lett. **18**, 3823 (2018).
[9] Y. C. Cheng, Q. Y. Zhang, and U. Schwingenschlögl, Phys. Rev. B **89**, 155429 (2014).
[10] R. Peng, Y. Ma, S. Zhang, B. Huang, and Y. Dai, J. Phys. Chem. Lett. **9**, 3612 (2018).
[11] N. Singh and U. Schwingenschlogl, Adv. Mater. **29**, 1600970 (2017).

[12] B. J. Wang, Y. Y. Sun, J. Chen, W. Ju, Y. P. An, and S. J. Gong, J. Mater. Chem. C **9**, 3562 (2021).

[13] W. Y. Tong, S. J. Gong, X. Wan, and C. G. Duan, Nat. Commun. **7**, 13612 (2016).

[14] C. Luo, X. Peng, J. Qu, and J. Zhong, Phys. Rev. B **101**, 245416 (2020).

[15] H. X. Cheng, J. Zhou, W. Ji, Y. N. Zhang, and Y. P. Feng, Phys. Rev. B **103**, 125121 (2021).

[16] P. Jiang, L. Kang, Y.-L. Li, X. Zheng, Z. Zeng, and S. Sanvito, Phys. Rev. B **104**, 035430 (2021).

[17] S. D. Guo, J. X. Zhu, W. Q. Mu, and B. G. Liu, Phys. Rev. B **104**, 224428 (2021).

[18] Y. F. Zhao, Y. H. Shen, H. Hu, W. Y. Tong, and C. G. Duan, Phys. Rev. B **103**, 115124 (2021).

[19] R. Peng, Y. Ma, X. Xu, Z. He, B. Huang, and Y. Dai, Phys. Rev. B **102**, 035412 (2020).

[20] W. Du, Y. Ma, R. Peng, H. Wang, B. Huang, and Y. Dai, J. Mater. Chem. C **8**, 13220 (2020).

[21] Y. Zang, Y. Ma, R. Peng, H. Wang, B. Huang, and Y. Dai, Nano. Res. **14**, 834 (2020).

[22] S. Li, J. He, L. Grajciar, and P. Nachtigall, J. Mater. Chem. C **9**, 11132 (2021).

[23] Q. Cui, Y. Zhu, J. Liang, P. Cui, and H. Yang, Phys. Rev. B **103**, 085421 (2021).

[24] H. Pan, Z. Li, C. C. Liu, G. Zhu, Z. Qiao, and Y. Yao, Phys. Rev. Lett. **112**, 106802 (2014).

[25] H. Hu, W. Y. Tong, Y. H. Shen, X. Wan, and C. G. Duan, npj Comput. Mater. **6**, 129 (2020).

[26] H. Huan, Y. Xue, B. Zhao, G. Gao, H. Bao, and Z. Yang, Phys. Rev. B **104**, 165427 (2021).

[27] S. Li, Q. Wang, C. Zhang, P. Guo, and S. A. Yang, Phys. Rev. B **104**, 085149 (2021).

[28] X. Feng, X. Xu, Z. He, R. Peng, Y. Dai, B. Huang, and Y. Ma, Phys. Rev. B **104**, 075421 (2021).

[29] Y. Wang and Y. Ding, Appl. Phys. Lett. **119**, 193101 (2021).

[30] X. Zhou, R.-W. Zhang, Z. Zhang, W. Feng, Y. Mokrousov, and Y. Yao, npj Comput. Mater. **7**, 160 (2021).

[31] G. Kresse and J. Hafner, Phys. Rev. B **49**, 14251 (1994).

[32] P. E. Blochl, Phys. Rev. B **50**, 17953 (1994).

[33] G. Kresse and J. Furthmuller, Phys. Rev. B **54**, 11169 (1996).

[34] J. P. Perdew, K. Burke, and M. Ernzerhof, Phys. Rev. Lett. **77**, 3865 (1996).

[35] S. L. Dudarev, G. A. Botton, S. Y. Savrasov, C. J. Humphreys, and A. P. Sutton, Phys. Rev. B **57**, 1505 (1998).

[36] V. I. Anisimov, J. Zaanen, and O. K. Andersen, Phys. Rev. B **44**, 943 (1991).

[37] Y. Zhang, L. F. Lin, A. Moreo, and E. Dagotto, Phys. Rev. B **105**, 085107 (2022).

[38] A. A. Mostofi, J. R. Yates, Y.-S. Lee, I. Souza, D. Vanderbilt, and N. Marzari, Comput. Phys. Commun. **178**, 685 (2008).

[39] X. Wang, J. R. Yates, I. Souza, and D. Vanderbilt, Phys. Rev. B **74**, 195118 (2006).

[40] C. Brouder, G. Panati, M. Calandra, C. Mourougane, and N. Marzari, Phys. Rev. Lett. **98**, 046402 (2007).

[41] M. P. López Sancho, J. M. López Sancho, and J. R. Rubio, J. Phys. F **14**, 1205 (1984).

[42] See Supplemental Material at http://link.aps.org/supplemental/10.1103/PhysRevB.105.195112 for the magnetic configurations; the band structures of SL RuClBr; and the evolution of the band structure of other systems, including SL $FeBr_2$, FeClBr, FeI_2, FeClI, and FeBrI.

[43] M. V. Fischetti and W. G. Vandenberghe, Phys. Rev. B **93**, 155413 (2016).

[44] W. Yao, D. Xiao, and Q. Niu, Phys. Rev. B **77**, 235406 (2008).

[45] D. Xiao, G. B. Liu, W. Feng, X. Xu, and W. Yao, Phys. Rev. Lett. **108**, 196802 (2012).

[46] R. Lv, J. A. Robinson, R. E. Schaak, D. Sun, Y. Sun, T. E. Mallouk, and M. Terrones, Acc. Chem. Res. **48**, 56 (2015).

[47] D. Xiao, M. C. Chang, and Q. Niu, Rev. Mod. Phys. **82**, 1959 (2010).

[48] M. H. Whangbo, E. E. Gordon, H. Xiang, H. J. Koo, and C. Lee, Acc. Chem. Res. **48**, 3080 (2015).

[49] M. H. Whangbo, H. Xiang, H. J. Koo, E. E. Gordon, and J. L. Whitten, Inorg. Chem. **58**, 11854 (2019).

[50] A. Rückriegel and P. Kopietz, Phys. Rev. B **95**, 104436 (2017).

[51] P. J. Chen, W. J. Li, and T. K. Lee, Phys. Rev. B **104**, 115161 (2021).

[52] X. Ma, L. Sun, J. Liu, and M. Zhao, Phys. Rev. B **104**, 155439 (2021).

[53] T. Jungwirth, Q. Niu, and A. H. MacDonald, Phys. Rev. Lett. **88**, 207208 (2002).

[54] Y. Yao, L. Kleinman, A. H. MacDonald, J. Sinova, T. Jungwirth, D. S. Wang, E. Wang, and Q. Niu, Phys. Rev. Lett. **92**, 037204 (2004).

[55] H. Pan, X. Li, H. Jiang, Y. Yao, and S. A. Yang, Phys. Rev. B **91**, 045404 (2015).